Three-Dimensional Semi-Finite Element Based Proximity Loss Calculation for Litz Wires in A High Frequency Transformer

Chaohui Liu, *Member, IEEE*, Xiao Chen, *Senior Member, IEEE*, Yakun Zhang, Shuai Shi, Zhaohe Meng, Zhichao Li and Wei Su

Abstract— Litz wires can be used to effectively reduce the skin effect loss while the proximity loss can be still significant considering the possible high flux densities produced by neighboring strands. This paper proposes a three-dimensional semi-finite element (semi-FE) based proximity loss calculation approach for Litz wires in a high frequency transformer. A set of analytical equations which are dedicated to the semi-FE approach for proximity loss calculations are derived. Compared to the existing semi-FE methods, the proposed method calculates proximity loss with volumetric factors in each element and hence can eliminate the error caused by the possible nonuniform mesh in winding regions. Experimental measurements show that compared to the conventional method, the proposed semi-FE method can predict closer proximity loss to measured results.

Index Terms—proximity loss, AC loss, Litz wire, semi-finite element, high frequency transformer

I. INTRODUCTION

HE power density of a transformer can be improved by increasing its electrical frequency. However, a higher electrical frequency leads to significantly higher AC copper loss which typically includes skin and proximity loss. Skin effect loss can be effectively reduced by using Litz wires whose diameter can be chosen to be smaller than the skin depth at operation frequency. However, the proximity loss can still be significant considering the possible high flux densities produced by neighboring strands [1, 2].

In the literature, various types of methods have been proposed to calculate the proximity loss of Litz wires, including one-dimensional (1D) or two-dimensional (2D) analytical method [3-8], finite element (FE) method [9], homogenization method [10-20] and semi-FE method [1-2, 21-23].

Ref. [3] used 1D current sheet to estimate AC losses in transformer windings, offering a quick estimation but with intrinsic errors if being used for round conductors. Bessel

functions were employed in [4] and [5] to provide a 2D analytical solution for the eddy currents in round conductors. To improve the accuracy of the analytical predictions of AC losses, more effects such as flux leakage in slot, fringing effects, and end effects, were incorporated into the analytical solutions in [6-8]. However, generally speaking, the accuracies of both flux density prediction and eddy current calculations of analytical methods are lower than numerical solutions, although analytical methods are more computationally efficient.

3D FE method was employed in [9] to calculate the AC losses of Litz wire considering twisting effects, albeit the computation time is highly demanding as each strand with fine mesh needs to be modelled.

The homogenization methods used in [10-20] can account for the eddy current reaction effect while taking less computation time by modelling windings as a homogenization region with frequency dependent properties. A generic finite element approach for homogenization in frequency domain was proposed in [17], which accounts for the local periodical effects of proximity losses and skin effects at macroscopic level. Ref. [18] developed closed form equations for equivalent complex permeabilities and conductivities to represent the proximity and skin effects for hexagonally packed wound coils. Ref. [19] proposed a proximity loss calculation method using 1D integral equation to solve the dipole magnetization generated by the anti-parallel eddy currents. It also showed that the calculated proximity loss agrees well with the direct FE method without the need for fine discretization. A closed form complex frequency-dependent proximity effect permeability was proposed in [20] to calculate proximity losses for Litz wires based on homogenization method with a wide frequency range. However, the homogenization method is based on an assumption that the magnetic field distribution over various strands is periodic in space. The accuracy of the

This work was supported in part by the National Key R&D Program (Grant No. 2021YFB2500600), and in part by Beijing Natural Science Foundation (Grant No. JQ23012).

Corresponding author: Chaohui Liu.

Chaohui Liu is with National New Energy Vehicle Technology Innovation Center, Beijing, China (e-mail: liuchaohui@nevc.com.cn).

Xiao Chen is with The University of Sheffield, Sheffield S1 3JD, United Kingdom (e-mail: xiao.chen@sheffield.ac.uk).

Yakun Zhang is with National New Energy Vehicle Technology Innovation Center, Beijing, China (e-mail: zhangyakun@nevc.com.cn).

Shuai Shi is with National New Energy Vehicle Technology Innovation Center, Beijing, China (e-mail: shishuai@nevc.com.cn).

Zhaohe Meng is with National New Energy Vehicle Technology Innovation Center, Beijing, China (e-mail: mengzhaohe@nevc.com.cn).

Zhichao Li is with National New Energy Vehicle Technology Innovation Center, Beijing, China (e-mail: lizhichao@nevc.com.cn).

Wei Su is with Beijing Electric Vehicle Co. Ltd., Beijing, China (e-mail: suwei@bjev.com.cn).

Color versions of one or more of the figures in this article are available online at http://ieeexplore.ieee.org

homogenization method may be compromised if the above assumptions are not satisfied.

Semi-FE methods were developed in [21-23] to use FE method to predict magnetic field distribution for Litz wires while employing analytical equation to calculate the proximity loss. Ref. [21] proposed a squared-field-derivative method to calculate proximity loss in Litz wires with round conductors, by using a simple magnetostatic FE solution combined with the proposed analytical equations. Eddy-current reaction field could not be considered in this method. Ref. [22] developed a coupled numerical and analytical method to calculate the Litz wire ohmic loss which is then coupled to a thermal model to allow both electromagnetic and thermal calculations for a transformer. The main approach of proximity loss calculation is the semi-FE method although the analytical equations are different from those in [21]. Ref. [23] proposed an efficient method to calculate AC loss for Litz wires and then implemented it in transient finite element analysis (FEA) of their software. Although homogenization is claimed in [23], the method they used is essentially the semi-FE method. Whereas the eddy-current reaction effect cannot be taken into account, the semi-FE method can predict the proximity loss with a reasonably good accuracy, particularly when the Litz wire diameter has been chosen to be smaller than the skin effect at the given operation frequency. However, when implementing the semi-FE method, without appropriately performing the spatial average of the squared-field-derivative, the users may produce a non-negligible error if there exists a nonuniform mesh in the winding region, particularly for the scenario that the users need to perform the post processing of the field solutions themselves if the commercial FEA tool does not provide required functions.

To avoid this error due to a possible nonuniform mesh in the winding region, this paper proposes a set of semi-FE dedicated equations to calculate proximity loss with volumetric factors in each element. Compared to the existing semi-FE methods in the literature, the proposed method in this paper explicitly includes the volumetric factors in the analytical equations and clearly demonstrates the large potential error in proximity loss calculations if those volumetric factors are not implemented while the mesh in the winding region is nonuniform.

II. 3D FE MODEL FOR SEMI-FE METHOD

A. Application background

The high frequency transformer studied in this paper is used in a CLLC resonant tank for an EV on-board battery charger whose schematic is shown in Fig. 1. The specifications of this EV charger and the parameters of the resonant tank are listed in Table I. More design details can be found in [2].

TABLE I

SPECIFICATIONS OF EV CHARGER AND RESONANT TANK [2]

Parameters	Symbol	Value	Unit
Input DC link voltage	V_{dc}	380	V
Input power rating	P_{in}	4.0	kW
Battery charging current	I_{bat}	9.0	A
Switching frequency range	f_{sw}	100-200	kHz
Battery rated capacity	$A \cdot h$	66.2	Ah
Battery fully charged voltage	V_{max}	403.2	V
Battery initial voltage	V_{min}	240	V
Series inductor	L_s	97.0	μН
Parallel/magnetic inductor	L_m	136.5	μΗ
Primary series capacitor	C_s	15.8	nF
Secondary series capacitor	C_{s2}	427	nF

TABLE II
PARAMETERS OF THE TRANSFORMER [2]

Parameters	Symbol	Value	Unit
Volume	V_e	44000	mm^3
Core area	A_{core}	363	mm^2
Primary turn number	N_{tp}	15	-
Secondary turn number	N_{ts}	9	-
Primary strand number	N_{sp}	38	-
Secondary strand number	N_{ss}	38	-
Primary strand diameter	d_{cp}	0.4	mm
Secondary strand diameter	d_{cs}	0.4	mm

B. FE Model

Semi-FE approach is used to estimate the Litz wire AC losses in this section. This approach combines FE method for flux density calculation and analytical equations for loss evaluation.

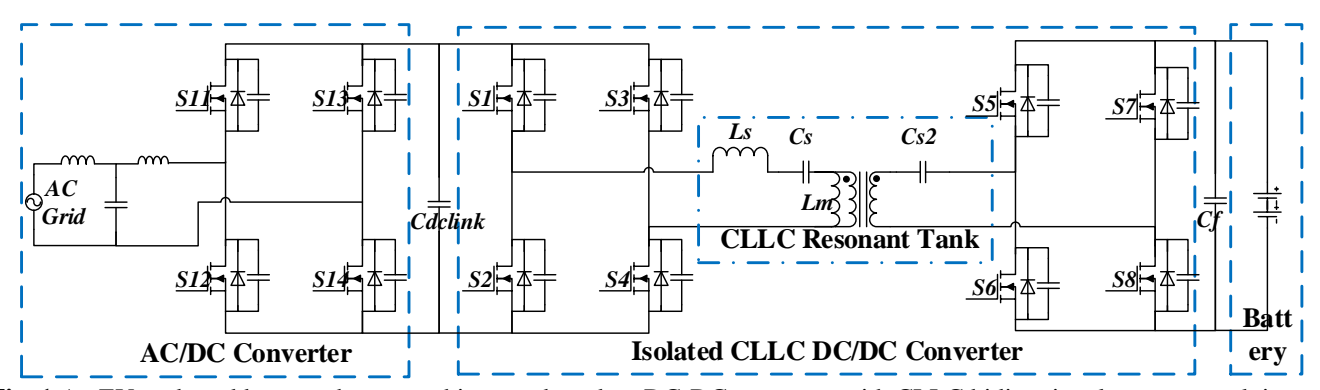


Fig. 1 An EV on-board battery charger architecture based on DC-DC converter with CLLC bidirectional resonant tank in which the high frequency transformer is studied in this paper [2].

To capture the 3D effect, 3D FE approach is adopted and the transformer geometry is shown in Fig. 2.

Taking advantage of the symmetrical behavior of the fields, only one fourth of the geometry needs to be modelled, as shown in Fig. 3, because the magnetic field is symmetric along the XOY and YOZ planes. These planes are defined in Fig. 3 (a). Tangent magnetic field and normal electric field are set as the boundary conditions along these planes. The model is built by extruding the 2D geometry in the ZOX plane, which has all the intersection points and lines of the 3D model projection. The 2D geometry has many areas, as seen in Fig. 3 (a). This model strategy helps generate regular mesh in a complex 3D geometry with arcs and narrow airgaps. The mesh densities on the core and winding are shown in Fig. 4.

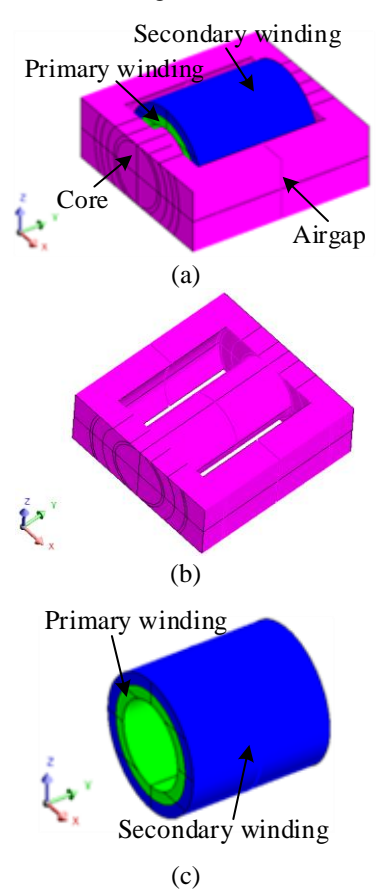


Fig. 2. 3D geometric model of the transformer geometries in FEA. (a) Winding and core. (b) Core. (c) Winding.

Note that the mesh on the surfaces parallel to ZOX plane are the same because we extrude the 3D model from the 2D model on ZOX plane and use the extrusion mesh generator. The material used for the transformer core is 3C92 whose B-H curve extracted from its datasheet can be seen in Fig. 5.

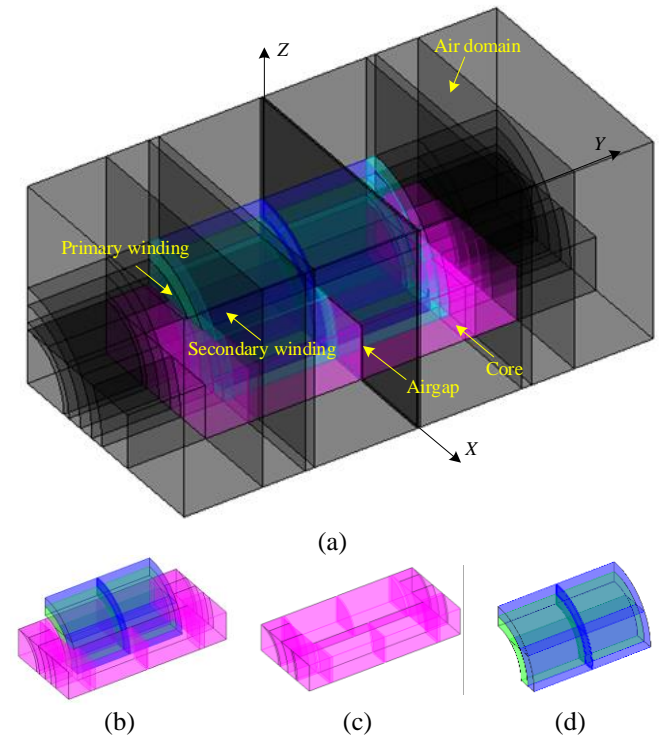


Fig. 3. Periodic 3D FE models of the transformer considering symmetries. (a) Full model. (b) Core, winding and airgap. (c) Core. (d) Winding.

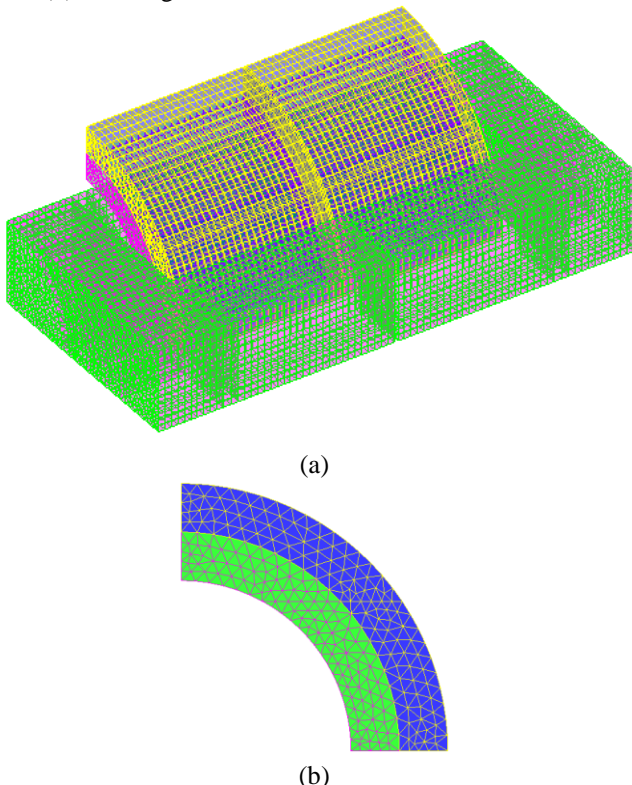


Fig. 4. Mesh density distribution of the 3D FE model. (a) Core and winding. (b) Cross section of the winding.

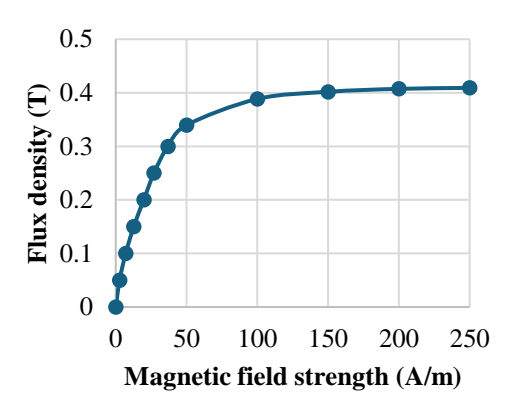


Fig. 5. B-H curve of the transformer core material 3C92 extracted from manufacturer's datasheet.

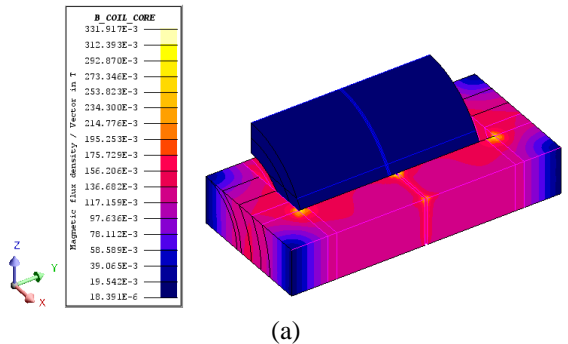
C. Nodal Flux Density

In this section, to account for the proximity effects in both primary and secondary windings, we run the 3D magnetostatic FEA with primary and secondary currents of (6A, 0A), (0A, 6A) and (6A, 6A). Their flux density distributions can be found in Fig. 6 to Fig. 8. Note that the flux densities calculated in FEA are vectors while Fig. 6 to Fig. 8 only show the distributions of the flux density modulus. The flux densities are higher at the winding corners near the airgap, especially the inner layer, as seen in Fig. 6 (c), Fig. 7 (c) and Fig. 8 (c). This is due to the fact that most of the flux leakage happens there due to the presence of airgap.

The peak flux density is higher at (6A, 0A) than at (0A, 6A) in that the primary winding has more turns (15 turns) than the secondary winding (9 turns). The peak flux density is lower at (6A, 6A) than at (6A, 0A) and (0A, 6A) in that the primary and secondary windings cancel some of the flux.

Then, the nodal flux densities at (6A, 0A), (0A, 6A) and (6A, 6A) are exported for the subsequent winding AC loss calculations.

Note that the eddy current effects in both windings and core are not considered because the 3D FEA used is magnetostatic. The raw unknowns calculated are the magnetic vector potentials which are further used to calculate the flux densities in x, y and z directions for all the nodes. Given that the magnetic circuit for the leakage flux in the winding region is nearly linear, the calculated flux densities at (6A, 0A), (0A, 6A) and (6A, 6A) are used as the reference to be scaled to work out the flux densities at other current excitations.



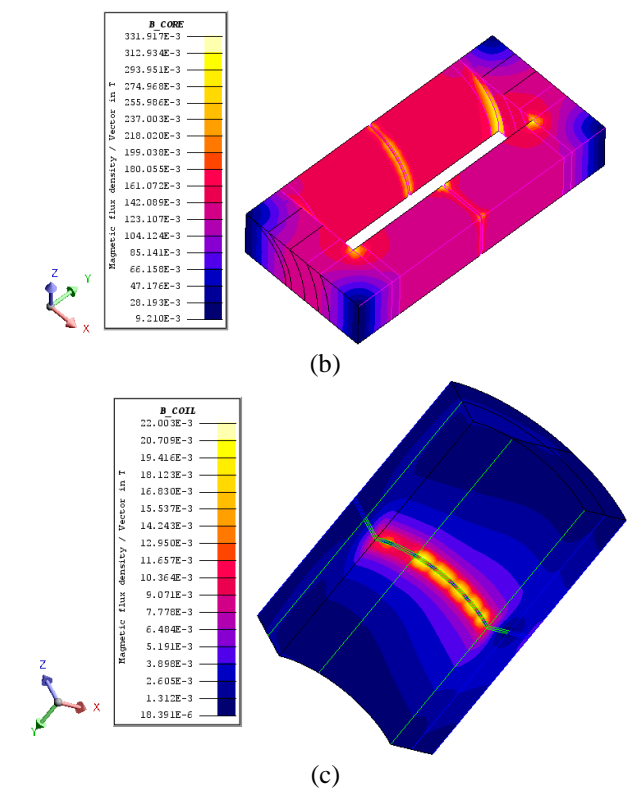
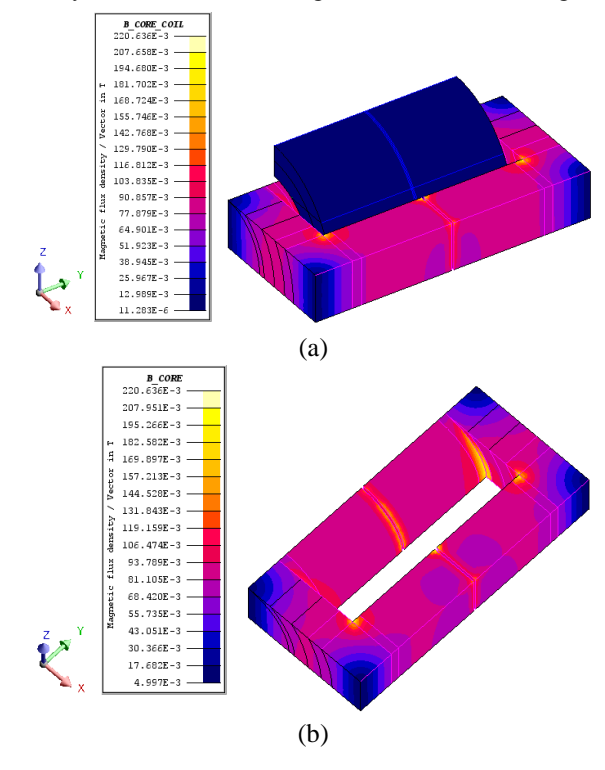


Fig. 6. Flux density distributions of the transformer core and winding at 6A current in the primary and 0A current in the secondary. (a) Core and winding. (b) Core. (c) Winding.



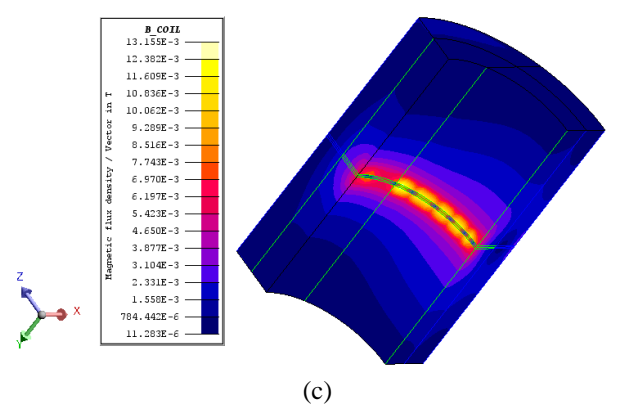


Fig. 7. Flux density distributions of the transformer core and winding at 0A current in the primary and 6A current in the secondary. (a) Core and winding. (b) Core. (c) Winding.

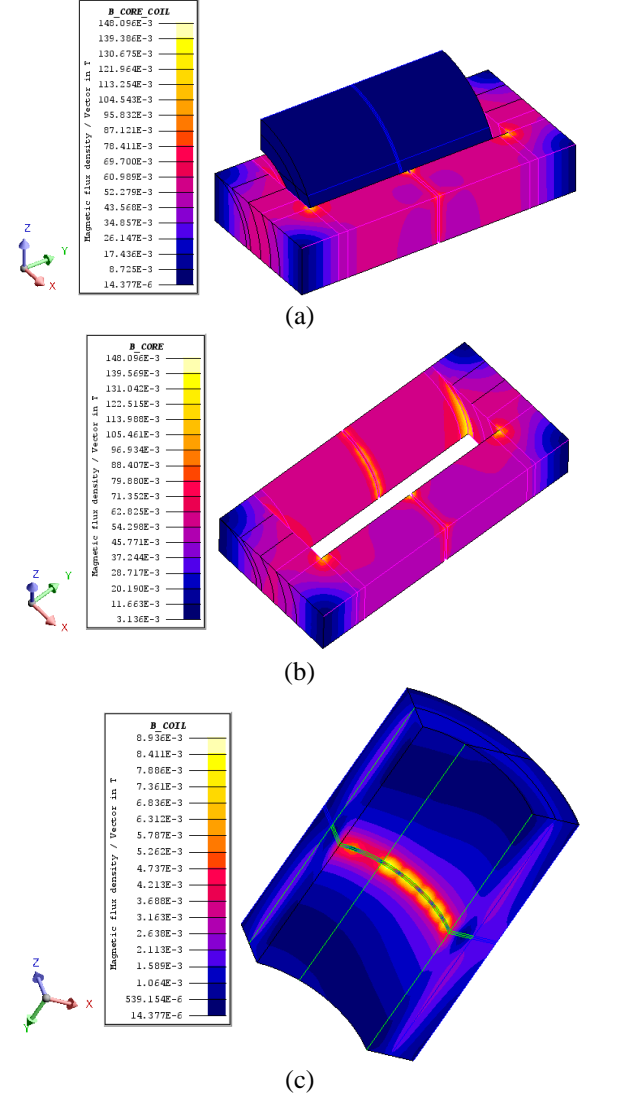


Fig. 8. Flux density distributions of the transformer core and winding at 6A current in the primary and 6A current in the secondary. (a) Core and winding. (b) Core. (c) Winding.

III. PROXIMITY LOSS CALCULATION

The proximity loss is the main part of the AC copper loss in this

application. Equation (1) from [21] can be used to calculate the transformer proximity loss, with the assumption that (a) the magnetic fields are perpendicular to the cylinder strand axis; (b) the strand diameter is not large compared to skin depth; (c) the eddy-current reaction fields are neglected; (d) hysteresis in the core does not affect the magnetic fields in the Litz wires; (e) equal current sharing between Litz wire strands; and (f) capacitive currents are negligible.

$$P_{px_trs} = \frac{\pi L_{tp} N_{tsp} d_{cp}^{4}}{64 \rho_{c}} \langle \left(\frac{d\vec{B}_{k}}{dt} \right)^{2} \rangle_{p} + \frac{\pi L_{ts} N_{tss} d_{cs}^{4}}{64 \rho_{c}} \langle \left(\frac{d\vec{B}_{n}}{dt} \right)^{2} \rangle_{s}$$

$$(1)$$

where L_{tp} and L_{ts} denote the average turn lengths in the primary and secondary windings respectively, N_{tsp} and N_{tss} are the number of turns per coil times the strand number of each turn in the primary and secondary windings respectively, d_{cp} and d_{cs} represent the strand diameters of the primary and secondary windings respectively, \vec{B}_k denotes flux density vector in the kth element of the primary winding, \vec{B}_n is the flux density vector in the nth element of the secondary winding, $\langle \cdot \rangle_p$ and $\langle \cdot \rangle_s$ are the spatial average operators over the primary and secondary windings respectively. Note that the flux densities shown in (1) are vectors as the magnetic fields in the windings resulting from the primary and secondary currents are three-dimensional. It should also be noted that Equation (1) needs to be time averaged over one cycle to work out the proximity loss. The effect of rotating fields due to the non-linear core has not been accounted for in this paper.

Given that the equivalent permeability for the leakage flux path in slot is remarkably low compared to the permeability in the core, the leakage flux density in the winding region is approximately linearly proportional to excitation current. Hence, \vec{B}_k in (1) can be calculated by the superposition of the magnetic fields due to the primary and secondary currents, as formulated in (2). Similarly, \vec{B}_n can be calculated using (3).

$$\vec{B}_k = \vec{B}_{pk} + \vec{B}_{sk} \tag{2}$$

$$\vec{B}_n = \vec{B}_{nn} + \vec{B}_{sn} \tag{3}$$

where \vec{B}_{pk} and \vec{B}_{sk} represent the flux density vectors in the kth element of the primary winding resulting from the primary and secondary currents, respectively, and \vec{B}_{pn} and \vec{B}_{sn} denote the flux density vectors in the nth element of the secondary winding resulting from the primary and secondary currents, respectively.

As per (2) and (3), the time averages of the squared derivative of the flux densities in the primary and secondary windings are derived to (4) and (5).

$$\langle \left(\frac{d\vec{B}_{k}}{dt} \right)^{2} \rangle_{p} = \langle \left| \frac{d\vec{B}_{pk}}{dt} \right|^{2} + \frac{d\vec{B}_{pk}}{dt} \cdot \frac{d\vec{B}_{sk}}{dt} + \left| \frac{d\vec{B}_{sk}}{dt} \right|^{2} \rangle_{p}$$

$$+ \frac{d\vec{B}_{sk}}{dt} \cdot \frac{d\vec{B}_{pk}}{dt} + \left| \frac{d\vec{B}_{sk}}{dt} \right|^{2} \rangle_{p}$$
(4)

$$\langle \left(\frac{d\vec{B}_n}{dt} \right)^2 \rangle_s = \langle \left| \frac{d\vec{B}_{pn}}{dt} \right|^2 + \frac{d\vec{B}_{pn}}{dt} \cdot \frac{d\vec{B}_{sn}}{dt} + \frac{d\vec{B}_{sn}}{dt} + \frac{d\vec{B}_{sn}}{dt} + \frac{d\vec{B}_{sn}}{dt} \rangle_s \tag{5}$$

For a given frequency of f, the current flowing in the primary winding can be represented by (6).

$$i_p = I_{pm} \sin(2\pi f t + \varphi_p) \tag{6}$$

where i_p denotes the instantaneous current of the primary winding, I_{pm} represents its amplitude, and φ_p is the initial phase angle. The current flowing in the secondary winding, i_s , can be expressed in a similar way.

Considering the magnetic field in the winding area is nearly linear with respect to the excitation current, the flux density at a reference current can be linearly scaled to predict the flux density at any other current. By way of example, Equation (7) can be used to work out the flux density in the kth element of the primary winding resulting from the primary current.

$$\vec{B}_{pk} = \frac{I_{pm}}{I_{0pm}} \vec{B}_{0pk} \tag{7}$$

where I_{0pm} is the amplitude of the reference primary current. \vec{B}_{0pk} represents the flux density vector in the kth element of the primary winding resulting from the reference primary current with amplitude I_{0pm} , as expressed in (8).

$$\vec{B}_{0pk} = \vec{B}_{0pkm} \sin(2\pi f t + \varphi_p) \tag{8}$$

where \vec{B}_{0pkm} denotes the flux density magnitude (magnitude over the time) vector in the kth element of the primary winding resulting from primary reference current with amplitude I_{0pm} .

Similar calculations can be performed for the flux density in the kth element of the primary winding \vec{B}_{sk} , and the flux densities in the nth element of the secondary winding resulting from the primary and secondary currents \vec{B}_{pn} and \vec{B}_{sn} .

Then, the derivative of \vec{B}_{pk} , \vec{B}_{sk} , \vec{B}_{pn} and \vec{B}_{sn} against time can be calculated. By way of example, Equation (9) expresses the derivative of \vec{B}_{pk} against time.

$$\frac{d\vec{B}_{pk}}{dt} = \frac{\vec{B}_{0pkm}}{I_{0mm}} \cdot \frac{di_p}{dt} \tag{9}$$

By substituting the derivative of \vec{B}_{pk} , \vec{B}_{sk} , \vec{B}_{pn} and \vec{B}_{sn} against time into (1) while considering the elementary weight factors, the proximity loss in the transformer can be predicted by (10).

$$\begin{split} &P_{px_trs} \\ &= \frac{\pi L_{tp} N_{tsp} d_{cp}^{4}}{64 \rho_{c} V_{olp}} \left[\langle \frac{\left| \vec{B}_{0pkm} \right|^{2}}{I_{0pm}^{2}} V_{k} \rangle_{p} \left(\frac{d \iota_{p}}{dt} \right)^{2} \right. \\ &+ \langle \frac{\vec{B}_{0pkm} \cdot \vec{B}_{0skm}}{I_{0pm} I_{0sm}} V_{k} \rangle_{p} \frac{d \iota_{p}}{dt} \cdot \frac{d \iota_{s}}{dt} \\ &+ \langle \frac{\vec{B}_{0skm} \cdot \vec{B}_{0pkm}}{I_{0sm} I_{0pm}} V_{k} \rangle_{p} \frac{d \iota_{s}}{dt} \cdot \frac{d \iota_{p}}{dt} \\ &+ \langle \frac{\left| \vec{B}_{0skm} \right|^{2}}{I_{0sm}^{2}} V_{k} \rangle_{p} \left(\frac{d \iota_{s}}{dt} \right)^{2} \right] \\ &+ \frac{\pi L_{ts} N_{tss} d_{cs}^{4}}{64 \rho_{c} V_{ols}} \left[\langle \frac{\left| \vec{B}_{0pnm} \right|^{2}}{I_{0pm}^{2}} V_{n} \rangle_{s} \left(\frac{d \iota_{p}}{dt} \right)^{2} \right. \\ &+ \langle \frac{\vec{B}_{0pnm} \cdot \vec{B}_{0snm}}{I_{0pm} I_{0sm}} V_{n} \rangle_{s} \frac{d \iota_{p}}{dt} \cdot \frac{d \iota_{p}}{dt} \\ &+ \langle \frac{\vec{B}_{0snm} \cdot \vec{B}_{0pnm}}{I_{0sm} I_{0pm}} V_{n} \rangle_{s} \frac{d \iota_{s}}{dt} \cdot \frac{d \iota_{p}}{dt} \\ &+ \langle \frac{\left| \vec{B}_{0snm} \right|^{2}}{I_{0sm} I_{0pm}} V_{n} \rangle_{s} \left(\frac{d \iota_{s}}{dt} \right)^{2} \right] \end{split}$$

where V_k represents the kth element's volume in the primary winding, V_n denotes the nth element's volume in the secondary winding, and V_{olp} and V_{ols} are the primary winding and the secondary winding volumes, respectively.

Hence, to calculate the proximity loss in the transformer, the following quantities need to be calculated by FEA, including $\langle \left| \vec{B}_{0pkm} \right|^2 \rangle_p$ which is the average flux density square of all the elements in the primary winding under the reference primary current excitation, $(|\vec{B}_{0skm}|^2)_p$ which is the average flux density square of all the elements in the primary winding under the reference secondary current excitation, $(|\vec{B}_{0pnm}|^2)_s$ which is the average flux density square of all the elements in the secondary winding under the reference primary current excitation, $\langle |\vec{B}_{0snm}|^2 \rangle_s$ which is the average flux density square of all the elements in the secondary winding under the reference secondary current excitation, $(\vec{B}_{0pkm} \cdot \vec{B}_{0skm})_p$ which is the average flux density product of all the elements in the primary winding under both the reference primary and secondary current excitations, and $(\vec{B}_{0pnm} \cdot \vec{B}_{0snm})_s$ which is the average flux density product of all the elements in the secondary winding under both the reference primary and secondary current excitations.

The winding elements may have different mesh sizes, and therefore the average flux density squares and products $\langle |\vec{B}_{0pkm}|^2 \rangle_p$, $\langle |\vec{B}_{0skm}|^2 \rangle_p$, $\langle |\vec{B}_{0pnm}|^2 \rangle_s$, $\langle |\vec{B}_{0snm}|^2 \rangle_s$, $\langle |\vec{B}_{0pkm} \cdot \vec{B}_{0skm} \rangle_p$ and $\langle |\vec{B}_{0pnm} \cdot \vec{B}_{0snm} \rangle_s$ over the winding elements may not reflect the true spatial average. To avoid potential error incurred by neglecting the elementary weight factors while using a nonuniform mesh, we use the weighted arithmetic mean of the element flux density squares and products, where the weights are the element volumes, as shown

in (10).

Equation (10) can be simplified into the products of matrices format, as expressed by (11).

$$P_{px_trs} = \overline{\left[\frac{d\iota_p}{dt} \quad \frac{d\iota_s}{dt}\right]} \mathbf{D} \begin{bmatrix} \frac{d\iota_p}{dt} \\ \frac{d\iota_s}{dt} \end{bmatrix}$$
(11)

where D matrix can be represented by (12).

$$\mathbf{D} = \gamma_{p} \left\langle \frac{\left| \vec{B}_{0pkm} \right|^{2}}{I_{0pm}^{2}} V_{k} \frac{\vec{B}_{0pkm} \cdot \vec{B}_{0skm}}{I_{0pm} I_{0sm}} V_{k} \right| \left\langle \frac{\vec{B}_{0skm} \cdot \vec{B}_{0pkm}}{I_{0sm} I_{0pm}} V_{k} \frac{\left| \vec{B}_{0skm} \right|^{2}}{I_{0sm}^{2}} V_{k} \right| + \gamma_{s} \left\langle \frac{\left| \vec{B}_{0pnm} \right|^{2}}{I_{0pm}^{2}} V_{n} \frac{\vec{B}_{0pnm} \cdot \vec{B}_{0snm}}{I_{0pm} I_{0sm}} V_{n} \right| \left\langle \frac{\vec{B}_{0snm} \cdot \vec{B}_{0pnm}}{I_{0sm} I_{0pm}} V_{n} \frac{\left| \vec{B}_{0snm} \right|^{2}}{I_{0sm}^{2}} V_{n} \right| \right\rangle_{s}$$
(12)

where coefficients γ_p and γ_s are shown in (13) and (14) respectively.

$$\gamma_{p} = \frac{\pi L_{tp} N_{tsp} d_{cp}^{4}}{64 \rho_{c} V_{olp}}$$

$$\gamma_{s} = \frac{\pi L_{ts} N_{tss} d_{cs}^{4}}{64 \rho_{c} V_{ols}}$$
(13)

$$\gamma_s = \frac{\pi L_{ts} N_{tss} d_{cs}^4}{64 \rho_c V_{ols}} \tag{14}$$

Equation (15) formulates the conventional equation of the winding DC loss P_{DC} in the transformer, based on Joule loss equation [24].

$$P_{DC} = \frac{1}{2} I_{pm}^2 R_{pDC} + \frac{1}{2} I_{sm}^2 R_{sDC}$$
 (15)

where R_{pDC} and R_{sDC} represent the DC resistances of the primary and secondary winding, and they can be predicted using (16) and (17) respectively.

$$R_{pDC} = \frac{4\rho_c L_{tp} N_{tsp}}{\pi d_{cp}^{2}}$$

$$R_{sDC} = \frac{4\rho_c L_{ts} N_{tss}}{\pi d_{cs}^{2}}$$
(16)

$$R_{SDC} = \frac{4\rho_c L_{ts} N_{tss}}{\pi d_{cs}^2} \tag{17}$$

Table III lists the winding proximity losses in the transformer at 6.22A and 6.5A RMS currents, based on (11) to (14). It can be seen that the proximity loss is the dominant loss component in the total copper losses.

TABLE III SUMMARY OF COPPER LOSSES IN THE TRANSFORMER

	Value		
Item	6.22A condition	6.5A condition	Unit
Total copper loss	24.65	26.92	W
Proximity loss total	24.05	26.27	W
Proximity loss primary	13.39	14.62	W
Proximity loss secondary	10.66	11.65	W
DC loss total	0.60	0.65	W
DC loss primary	0.19	0.20	W
DC loss secondary	0.41	0.45	W
Primary current	6.22	6.50	A
Secondary current	10.37	10.83	A

IV. IMPACT OF NONUNIFORM MESH

It should be noted that the volumetric factors V_k , V_n , V_{olp} and V_{ols} need to be considered in order to avoid the error caused by a possible nonuniform mesh in the primary and secondary winding regions. This section investigates the impact of nonuniform mesh on the errors incurred by neglecting the aforementioned volumetric factors.

Fig. 9 illustrates the mesh densities in the cross-sections of primary and secondary windings at various levels of nonuniformities, where k is defined as the ratio of the circumferential segment number on the inner bore of the primary winding to that of the outer bore of the primary winding. By way of example, the mesh density used in the calculations in Section III has a k=1.05, as the primary winding inner bore has 22 segments at circumferential direction while its outer bore has 21 segments at circumferential direction, as illustrated in Fig. 9 (c). In the five models shown in Fig. 9, the number of segments on the outer bore of the primary winding (the boundary between primary and secondary windings) keeps being 21, while the number of segments on the inner bore of the primary winding varies from 7 to 66, corresponding to a variation of k from 0.33 to 3.14. Note that some asymmetry in the mesh exists at the circumferential direction due to the fact that each arc in Fig. 9 consists of two arcs separated by a horizontal line in order to generate more controlled mesh in the

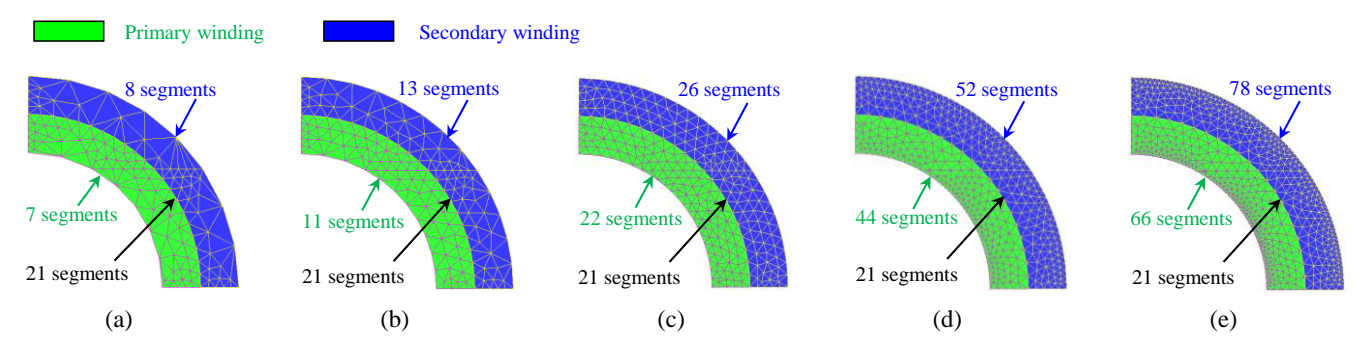


Fig. 9 Mesh density illustration in the cross-sections of primary and secondary windings at various levels of nonuniformities. (a) k=0.33. (b) k=0.52. (c) k=1.05. (d) k=2.10. (e) k=3.14.

air gaps between windings and cores.

By using the proposed proximity loss calculation approach in Section III, the predicted proximity losses with and without considering volumetric factors (V_k, V_n, V_{olp}) and V_{ols} at various levels of mesh nonuniformities are compared in Fig. 10. It can be seen that with the increase of k, the proximity loss with volumetric factors coverages to 26.3W after $k \ge 0.52$, which is consistent with the fact that after the mesh density beyond a threshold a denser mesh does not improve the accuracy of FEA results. However, if the volumetric factors are ignored, it can be seen that the calculated proximity loss varies significantly with the level of mesh nonuniformity. Fig. 11 shows the incurred errors of proximity loss calculations if volumetric factors are ignored with respect to those with volumetric factors, i.e. the relative difference between the proximity losses without volumetric factors and those with volumetric factors. The mesh used for calculations in Section III, i.e. Fig. 9 (c), exhibits the lowest error, i.e. -3.3%, as it has the most uniform mesh among the five models shown in Fig. 9. It also shows that when k increases or decreases from the reference point (k=1.05), the absolute values of those errors increase, because the level of mesh nonuniformity increases. By way of example, if k=0.33, corresponding to Fig. 9 (a), the error in proximity loss can reach 17.2% if the volumetric factors are neglected. This mesh density is less likely in reality considering the quality of mesh is relatively poor. However, when k=3.14, corresponding to Fig. 9 (e), the mesh density is much denser, but this cannot guarantee an accurate prediction of proximity losses if the volumetric factors are ignored. Indeed, its error reaches -30.6% if the volumetric factors are not considered. This demonstrates that the volumetric factors are essential to be accounted for in the proposed proximity loss calculation method with Semi-FE approach.

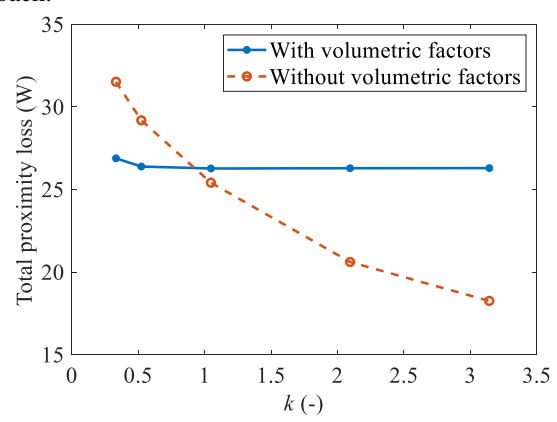


Fig. 10 Comparison of proximity losses with and without considering volumetric factors at various levels of mesh nonuniformities.

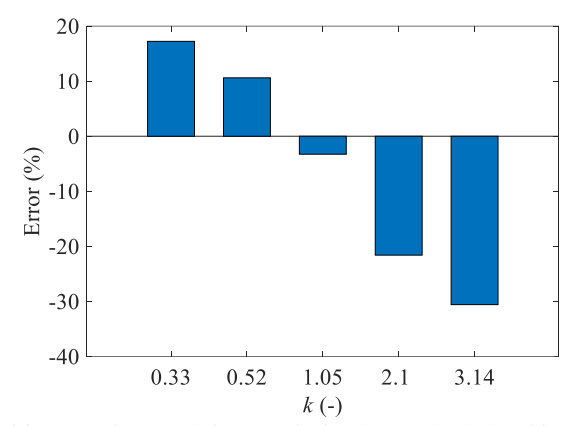


Fig. 11 Errors incurred for proximity loss calculation if volumetric factors are ignored at various levels of mesh nonuniformities.

V. EXPERIMENTAL MEASUREMENTS

A. Power Loss Measurements

The transformer is installed in a CLLC resonant converter operating in the vehicle-to-grid (V2G) reverse mode for an electric vehicle application. The voltage and current waveforms are measured using an oscilloscope before estimating the transformer total power loss by subtracting the primary side power from the secondary side power.

The test rig setup is shown in Fig. 12 and the prototype bidirectional charger is shown in Fig. 13. A variac is used to provide an adjustable AC input to the charger. A front-end AC/DC converter converts AC into DC and vice versa, and regulates the DC link voltage to ~380V. The DC power is controlled by the CLLC resonant converter for battery charging and discharging operations. Both the front-end and CLLC resonant converters are controlled by the NI Compact RIO 9082 digital controller from National Instruments.



Fig. 12 Test rig setup.

The measurement of the transformer voltages and currents performance is performed at the following operation conditions: the battery voltage is 238.33V, the DC link voltage is 383.7V, the discharging current is 9.0A, and the switching frequency is approximately 125.94kHz.

The measured voltages and currents of the transformer are obtained from the waveform data of the oscilloscope and

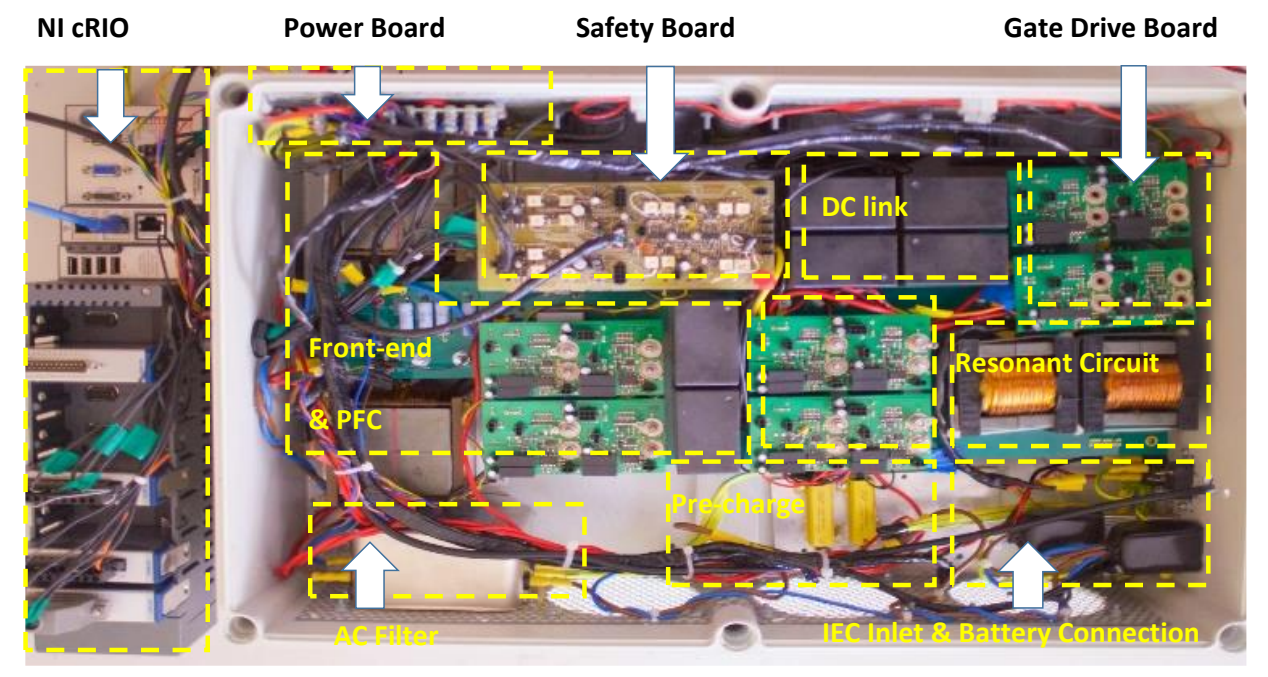


Fig. 13 Prototype of the converter with high frequency transformer.

plotted in Fig. 14. Then the power loss in the transformer can be calculated using the secondary side power subtracting the primary side power in the V2G reverse mode.

As observed in Fig. 14, the secondary side current is lagging the chopped voltage due to the zero-voltage-switching operation. The secondary current waveform is close to sinusoidal, despite a small flat area in the discontinuous current mode operation, because of the operating frequency close to (slightly below) the series resonant frequency. The primary side current (the current through the rectifier diodes) shows the rectifier diodes turned off at zero-current-switching operation with low di/dt. The primary side voltage is not pure square wave but has a voltage drop owing to the leakage inductance, resonant tank and equivalent winding resistance.

The sampling rate of the oscilloscope is 100MS/s (corresponding resolution 1E-8). The switching frequency is 125.94 kHz, and thus 800 sample points are recorded in one switching cycle. The instantaneous secondary and primary side power at each sampling time is calculated with the instantaneous voltage and current, and then the averaged transformer power loss in one switching cycle is calculated as the subtraction of the power in the two sides of the transformer. Hence, in this test, the power through the transformer can be calculated to be 2092.28 - 2066.65 = 25.63W.

Given that the primary and secondary winding currents exhibit higher order harmonics as indicated in Fig. 14, Fast Fourier Transform (FFT) has been used to extract the current harmonics before working out the proximity losses using the proposed Semi-FE method for each harmonic. Considering the leakage flux density in the winding region is approximately linearly proportional to excitation current, the proximity loss calculations for all the harmonics can be performed using one FE-predicted magnetic field distribution at a reference current.

The total number of harmonics considered in this calculation is up to 30th order which correlates to a 3.8MHz frequency range. The sum of proximity losses caused by the currents from fundamental to 30th order harmonics for primary and secondary windings are 11.70W and 9.32W respectively. The total DC loss for both windings is 0.56W. Hence, the total copper loss in the transformer is 21.58W. The core loss is calculated by using semi-FE method with Steinmetz's equation [25], i.e. substituting the nodal flux density and element size extracted from FEA to the classical Steinmetz's equation [25] and calculating the total core loss of all the elements of the core. The calculated core loss is 9.169W. Hence, the total power loss in the transformer is 30.75W.

For comparison, the conventional method using (1) [21] with predicted spatial average flux densities of the primary and secondary windings while assuming sinusoidal current excitations is applied to estimate the transformer copper loss. Instead of using element-by-element calculation of the proximity loss, the conventional method referred in this paper uses the average flux densities of the primary and secondary windings to calculate lumped proximity losses for primary and secondary windings. The resultant copper loss is 29.80W. The core loss calculation uses the same method described in the above paragraph, i.e. semi-FE method with Steinmetz's equation, given that the core loss is not the focus of this paper. Hence, the core loss calculated here is also 9.169W and thus the total loss is 34.80W.

The comparison of the two methods with respect to the measured results is shown in Table IV. As can be observed, the resultant copper loss from Semi-FE model is 21.58W, 31.1% more than the measured results 16.46W. This difference may be caused by the measurement inaccuracy. Since the switching frequency is quite high, only 800 samples are recorded in one

switching cycle, thus even a small phase delay in the inductor voltage and current will cause a big error. However, the copper loss estimated by the conventional method is 29.80W, which is 81.0% more than the measured results. The semi-FE method is clearly more accurate than the conventional method using an average flux density.

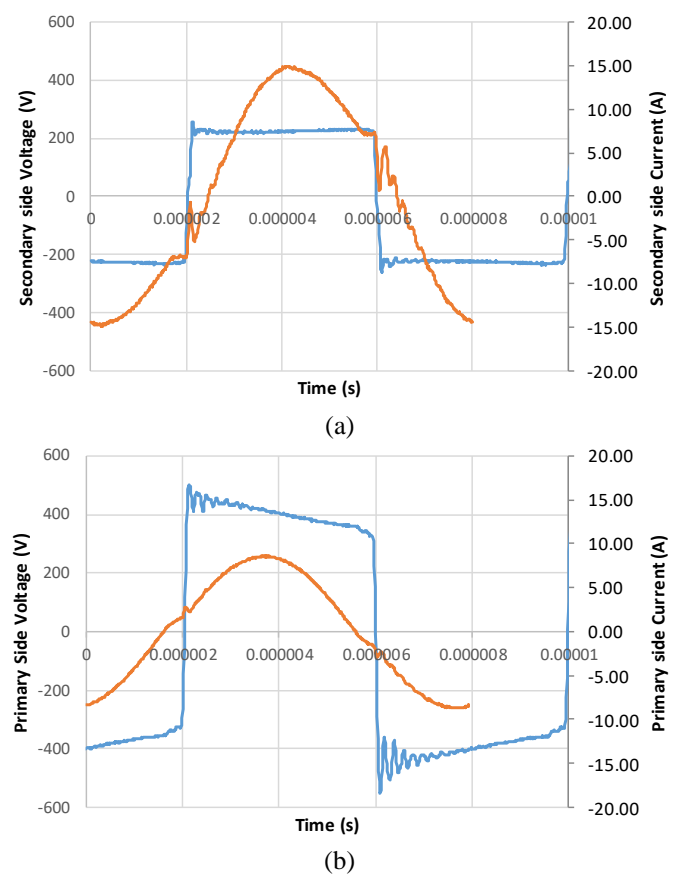


Fig. 14 The transformer voltage (in blue) and current (in orange) in the (a) secondary side and (b) primary side.

TABLE IV
COMPARISON OF LOSS PREDICTION WITH VARIOUS
METHODS

Item	Measured	Semi-FE	Conventional	Unit
Total loss	25.63	30.75	38.97	W
Copper loss	16.46	21.58	29.80	W
Copper loss difference against measurement	-	31.1%	81.1%	-

B. AC Resistance Measurements

In this sub-section, impedance measurements are performed to measure the AC resistances of the primary and secondary windings over various frequencies, using a precision impedance analyzer, Wayne Kerr 6500B whose bandwidth is 50MHz and impedance measurement accuracy is $\pm 0.05\%$. Given that no auxiliary transformers with 1:1 turn ratio or zero gap have been

prepared, the measurement results shown in this sub-section cannot serve as a validation of the AC resistances associated with the proximity loss calculations presented in Section III. Instead, it shows the comparison of the measured equivalent series resistances (ESR) and the predicted self-resistances based on the proximity loss calculations shown in Section III.

The experimental setup is shown in Fig. 15. Impedance measurements are performed for both primary and secondary windings over 100Hz-150kHz with their own excitations only. In other words, when measuring the impedances of the primary winding, the secondary winding is not excited. On the other hand, when measuring the impedances of the secondary winding, the primary winding is not excited. Meanwhile, considering the presence of the iron losses in the soft magnetic core, the real part of the measured impedance in this sub-section is a combination of the self-resistance, the equivalent resistance for core loss, and the equivalent resistance due to capacitance effect

Using the 1^{st} and 4^{th} elements of the **D** matrix shown in (11) and (12), Section III, i.e. D_{11} and D_{22} , the self-resistances for primary and secondary windings can be calculated by converting their corresponding proximity losses into equivalent resistances based on Joule's Law.

Fig. 16 shows the comparison of the predicted self-resistance and measured ESR for both primary winding and secondary winding. It can be seen that there is an obvious difference between the predicted self-resistance and measured ESR for both primary and secondary windings. This is because, as mentioned above, the measured ESR is a combination of the self-resistance, the equivalent resistance for core loss, and the equivalent resistance due to capacitance effect, while the predicted self-resistance does not account for the core loss effect and capacitance effect on the equivalent resistance.

At 125kHz, the operation frequency shown in Section V.A, the predicted self-resistances for the primary and secondary windings are 0.284Ω and 0.120Ω , respectively, which are 21.8% and 25.4% lower than the measured ESRs for the primary and secondary windings 0.363Ω and 0.161Ω , respectively. Those 21.8% and 25.4% differences are close to the 20% error range reported in [26] if the core loss effect is neglected.

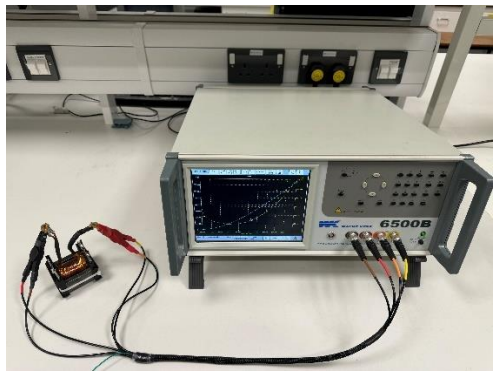


Fig. 15 Experimental setup for the impedance measurements of the primary and secondary windings of the transformer.

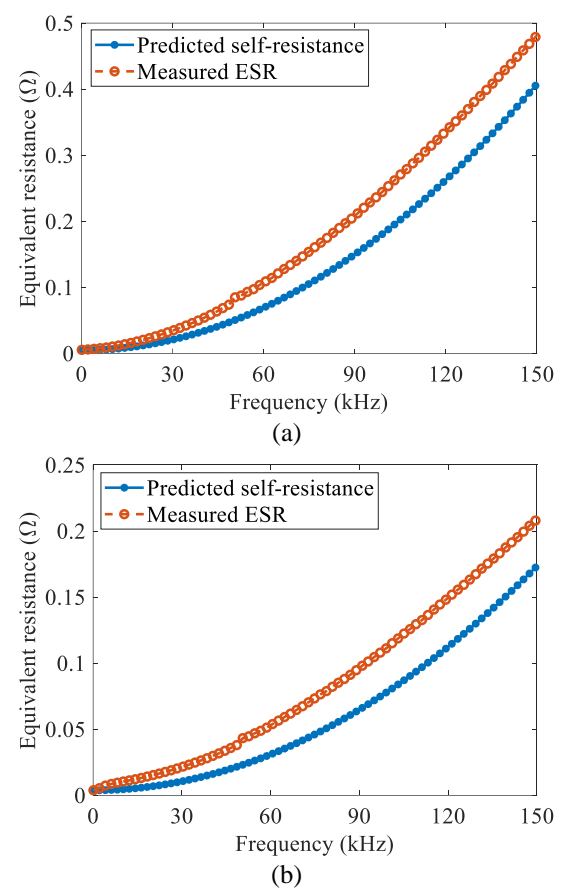


Fig. 16 Comparison of the predicted self-resistance and measured equivalent series resistance (ESR). (a) Primary winding. (b) Secondary winding.

Note that in order to precisely validate the AC resistance for a transformer, auxiliary transformers with 1:1 turn ratio and zero gap are usually needed to measure both self-resistance and mutual resistance while separating the core loss effect from the measured real part of impedance [26-28]. Due to the absence of those auxiliary transformers, this paper only compares the measured ESR and the predicted self-resistances, for the sake of cross checking the trends and relative difference between those quantities.

VI. CONCLUSION

This paper proposes a 3D semi-FE based proximity loss calculation method for Litz wires in a high frequency transformer. By explicitly including the volumetric factors into an existing proximity loss model in the literature, a set of analytical equations which are dedicated to the semi-FE approach for proximity loss calculations are derived. The proposed method can eliminate the error caused by the possible nonuniform mesh in winding regions. Experimental measurements have been performed and it shows that the proposed proximity loss calculation method predicts copper losses closer to the experimental results than the conventional method using an average flux density.

The contribution to knowledge includes (a) it explicitly included the volumetric factors in the analytical equations of

proximity loss calculations, which can help the users run the correct spatial average of the squared derivative of the flux densities in a separate programming environment if some commercial FEA tools do not provide the necessary functions; (b) it revealed and quantified the possible errors in proximity loss calculations at various levels of mesh nonuniformity if using semi-FE methods while neglecting the volumetric factors in each element.

ACKNOWLEDGEMENTS

The author would like to appreciate Professor Jiabin Wang, Dr Chris Gould, Dr Bhaskar Sen at the University of Sheffield for their administrative and technical support.

REFERENCES

- [1] C. Liu et al., "Three-Dimensional Semi-Finite Element Based Proximity Loss Calculation for Litz Wires in A High Frequency Transformer," 2023 IEEE Energy Conversion Congress and Exposition (ECCE), Nashville, TN, USA, 2023, pp. 2783-2788.
- [2] C. Liu, "Analysis, Design and Control of DC-DC Resonant Converter for On-board Bidirectional Battery Charger in Electric Vehicles," PhD thesis, University of Sheffield, 2017.
- [3] P. L. Dowell, "Effects of eddy currents in transformer windings," Proceedings of the Institution of Electrical Engineers, vol. 113, no. 8, 1966.
- [4] J. A. Ferreira, "Improved analytical modeling of conductive losses in magnetic components," in IEEE Transactions on Power Electronics, vol. 9, no. 1, pp. 127-131, Jan. 1994.
- [5] M. Albach, "Two-dimensional calculation of winding losses in transformers," 2000 IEEE 31st Annual Power Electronics Specialists Conference, 2000, pp. 1639-1644 vol.3.
- [6] F. Tourkhani and P. Viarouge, "Accurate analytical model of winding losses in round Litz wire windings," IEEE Transactions on Magnetics, vol. 37, no. 1, pp. 538-543, 2001.
- [7] N. Xi and C. R. Sullivan, "An improved calculation of proximity-effect loss in high-frequency windings of round conductors," in IEEE 34th Annual Conference on Power Electronics Specialist, Acapulco, Mexico, 2003, vol. 2: IEEE, pp. 853-860.
- [8] N. J. Salk and C. M. Cooke, "Calculation of AC Losses in Multi-phase Litz Coil Systems," 2022 IEEE Transportation Electrification Conference & Expo (ITEC), Anaheim, CA, USA, 2022, pp. 594-599.
- [9] E. Plumed, J. Acero, I. Lope and C. Carretero, "3D Finite Element Simulation of Litz Wires with Multilevel Bundle Structure," IECON 2018 - 44th Annual Conference of the IEEE Industrial Electronics Society, Washington, DC, USA, 2018, pp. 3479-3484.
- [10]J. Gyselinck and P. Dular, "Frequency-domain homogenisation of bundles of wires in 2-D magnetodynamic FE calculations," in IEEE Transactions on Magnetics, vol. 41, no. 5, pp. 1416-1419, May 2005.
- [11]A. D. Podoltsev, K. G. N. B. Abeywickrama, Y. V. Serdyuk and S. M. Gubanski, "Multiscale Computations of Parameters of Power Transformer Windings at High Frequencies. Part I: Small-Scale Level," in IEEE Transactions on Magnetics, vol. 43, no. 11, pp. 3991-3998, Nov. 2007.
- [12]J. -R. Sibue, J. -P. Ferrieux, G. Meunier and R. Periot, "Modeling of Losses and Current Density Distribution in Conductors of a Large Air-Gap Transformer Using Homogenisation and 3-D FEM," in IEEE Transactions on Magnetics, vol. 48, no. 2, pp. 763-766, Feb. 2012.
- [13]J. Gyselinck, R. V. Sabariego and P. Dular, "Time-Domain Homogenisation of Windings in 2-D Finite Element Models," in IEEE Transactions on Magnetics, vol. 43, no. 4, pp. 1297-1300, April 2007.
- [14]R. V. Sabariego, P. Dular and J. Gyselinck, "Time-Domain Homogenisation of Windings in 3-D Finite Element Models," in IEEE Transactions on Magnetics, vol. 44, no. 6, pp. 1302-1305, June 2008.
- [15]D. Lin, C. Lu, N. Chen and P. Zhou, "An Efficient Method for Litz-Wire AC Loss Computation in Transient Finite Element Analysis," in IEEE Transactions on Magnetics, vol. 58, no. 5, pp. 1-10, May 2022.
- [16]H. Igarashi, "Semi-Analytical Approach for Finite-Element Analysis of Multi-Turn Coil Considering Skin and Proximity Effects," in IEEE Transactions on Magnetics, vol. 53, no. 1, pp. 1-7, Jan. 2017.
- [17] G. Meunier, V. Charmoille, C. Guerin, P. Labie and Y. Marechal, "Homogenization for Periodical Electromagnetic Structure: Which

> REPLACE THIS LINE WITH YOUR MANUSCRIPT ID NUMBER (DOUBLE-CLICK HERE TO EDIT) <

Formulation?," in IEEE Transactions on Magnetics, vol. 46, no. 8, pp. 3409-3412, Aug. 2010.

[18]D. C. Meeker, "An improved continuum skin and proximity effect model for hexagonally packed wires," in Journal of Computational and Applied Mathematics, vol. 236, no. 18, pp. 4635-4644, Dec. 2012.

[19]S. Hiruma and H. Igarashi, "Fast 3-D Analysis of Eddy Current in Litz Wire Using Integral Equation," in IEEE Transactions on Magnetics, vol. 53, no. 6, pp. 1-4, June 2017.

[20]K. Niyomsatian, J. Gyselinck, R. V. Sabariego, "Closed-form complex permeability expression for proximity-effect homogenisation of litz-wire windings," in IET Science, Measurement & Technology, vol. 14, no. 3, p. 287-291, Mar 2020.

[21]C. R. Sullivan, "Computationally efficient winding loss calculation with multiple windings, arbitrary waveforms, and two-dimensional or threedimensional field geometry," in IEEE Transactions on Power Electronics, vol. 16, pp. 142-150, 2001.

[22]A. Roßkopf, C. Joffe and E. Bär, "Calculation of ohmic losses in litz wires by coupling analytical and numerical methods," 2014 4th International Electric Drives Production Conference (EDPC), 2014, pp. 1-6.

[23]D. Lin, C. Lu, N. Chen and P. Zhou, "An Efficient Method for Litz-Wire AC Loss Computation in Transient Finite Element Analysis," in IEEE Transactions on Magnetics, vol. 58, no. 5, pp. 1-10, May 2022.

[24] The Scientific Papers of James Prescott Joule (no. v. 1). Cambridge University Press, 1884.

[25]C. P. Steinmetz, "On the law of hysteresis," in Proceedings of the IEEE, vol. 72, no. 2, pp. 197-221, Feb. 1984.

[26]B. X. Foo, A. L. F. Stein and C. R. Sullivan, "A step-by-step guide to extracting winding resistance from an impedance measurement," 2017 IEEE Applied Power Electronics Conference and Exposition (APEC), Tampa, FL, USA, 2017, pp. 861-867.

[27]K. Niyomsatian, J. J. C. Gyselinck and R. V. Sabariego, "Experimental Extraction of Winding Resistance in Litz-Wire Transformers—Influence of Winding Mutual Resistance," in IEEE Transactions on Power Electronics, vol. 34, no. 7, pp. 6736-6746, July 2019.

[28]T. Chen, Z. Zhao, Z. Shen, H. Jia, J. Ji and H. Wang, "Litz-Wire Winding Loss Calculation Method for Optimal Design of High-Frequency Transformers," in IEEE Journal of Emerging and Selected Topics in Power Electronics, vol. 12, no. 2, pp. 2027-2040, April 2024.

Chaohui Liu received the B.E. from North University of China, M.E from Beihang University, and Ph.D. in the Electrical Machines and Drives (EMD) Research Group from the University of Sheffield, UK in 2006, 2011 and 2017 respectively.

From 2017 to 2020, he was with the Department of Research, Design and Development, Dyson Technology Limited, UK, where he was appointed an Advanced Engineer in 2017 and Senior Engineer in 2018

He is currently a Principal Engineer and the Head of Powertrain at National New Energy Vehicle Technology Innovation Center (NEVC), Beijing, China. His research interests include machine drive, advanced control strategy, power converters, electric vehicle battery charger, wide band-gap device packaging and power module applications.



Xiao Chen received BEng and MSc degrees in electrical engineering from Harbin Institute of Technology, China, in 2009 and 2011, respectively, and PhD degree in electrical machines from University of Sheffield, in 2015. He was a research associate at University of Sheffield, from Jan 2016 to May 2018, before working as an advanced motor drive engineer in Dyson, UK, from July 2018 to Sep 2019. Since Sep 2019, He rejoined Electrical Machines and Drives group at University of Sheffield and is now a

senior lecturer in electrical machines.

His current research interests include high frequency bearing currents, manufacturing impact on electrical machine performances, high-speed electrical machines, digital twin of electrical machine and drive, multi-physics modelling of electrical machines, etc.



Yakun Zhang received the B.E. degree in mechanical manufacturing and automation from the North China Institute of Aerospace Engineering, Langfang, China, in 2019, and the M.E. degree in mechanics from the Beijing University of Technology, Beijing, China, in 2022. She is currently a Research Engineer with National New Energy Vehicle Technology Innovation Center. Her main research interests include packaging structure design and advanced packaging technology development of automotive power electronics.



Shuai Shi received the M.Sc degree from China University of Mining and Technology-Beijing in 2017. He is skilled in finite element numerical simulation and has 8 years of work experience. Currently, he is employed as a thermal design engineer at the Beijing National New Energy Vehicle Technology Innovation Center. His research interests include fluid heat transfer, advanced packaging and SIC inverters.



Center, Beijing, China. He has been engaged in the development of motor controllers for sixteen years and has rich experience in motor controller development. He was with HollySys, Goldwind, CEPRI, and National New Energy Vehicle Technology Innovation Center, respectively, gaining knowledge on the machine drive, and drive inverters. His research interests include power inverters, IGBT and SiC

Zhaohe Meng is currently a Hardware Engineer with

National New Energy Vehicle Technology Innovation

drivers.



Zhichao Li is currently a Software Engineer with National New Energy Vehicle Technology Innovation Center, Beijing, China. He has been engaged in the development of new energy vehicle motor controllers for ten years and has rich experience in motor controller development. He was with TM4, JJE, BJEV, and National New Energy Vehicle Technology Innovation Center, respectively, gaining knowledge on the machine drive, and drive inverters. His research interests include machine drive, drive inverters,

control strategies for EV IGBT and SiC inverters.



Wei Su received the B.E. from the School of Mechanical Engineering in 2006. He continued his studies from 2016 to 2019 and received the M.E. degree in Vehicular Engineering at the Beijing Institute of Technology. Currently, he is the Director and Chief Engineer of the Electric Drive System Department at the Beijing Automotive Research Institute. His main research interests are electric drive powertrains, motor design, and motor controller algorithms.